The EDR inflow region of a reconnecting current sheet in the geomagnetic tail

Cite as: Phys. Plasmas **29**, 052903 (2022); https://doi.org/10.1063/5.0083169
Submitted: 22 December 2021 • Accepted: 19 April 2022 • Published Online: 06 May 2022

J. L. Burch, M. Hesse, J. M. Webster, et al.

Physics of Plasmas ARTICLE scitation.org/journal/php

The EDR inflow region of a reconnecting current sheet in the geomagnetic tail

Cite as: Phys. Plasmas **29**, 052903 (2022); doi: 10.1063/5.0083169
Submitted: 22 December 2021 · Accepted: 19 April 2022 ·
Published Online: 6 May 2022

View Online Export Citation CrossMark

J. L. Burch,[1,a)] M. Hesse,[2] J. M. Webster,[3] K. J. Genestreti,[4] R. B. Torbert,[4,5] R. E. Denton,[6] R. E. Ergun,[7] B. L. Giles,[8] D. J. Gershman,[8] C. T. Russell,[9] S. Wang,[10] L.-J. Chen,[8] K. Dokgo,[1] K.-J. Hwang,[1] and C. J. Pollock[11]

AFFILIATIONS

[1]Southwest Research Institute, San Antonio, Texas 78238, USA
[2]NASA Ames Research Center, Moffett Field, California 94035, USA
[3]Rice University, Houston, Texas 77005, USA
[4]Southwest Research Institute, Durham, New Hampshire 03824, USA
[5]University of New Hampshire, Durham, New Hampshire 03824, USA
[6]Dartmouth College, Hanover, New Hampshire 03755, USA
[7]LASP, University of Colorado, Boulder, Colorado 80303, USA
[8]NASA Goddard Space Flight Center, Greenbelt, Maryland 20771, USA
[9]University of California, Los Angeles, California 90095, USA
[10]University of Maryland, College Park, Maryland 20742, USA
[11]Denali Scientific, Fairbanks, Alaska 99743, USA

Note: This paper is a part of the Special Collection: Plasma Physics from the Magnetospheric Multiscale Mission.
[a)]**Author to whom correspondence should be addressed:** jburch@swri.edu

ABSTRACT

On 6 July 2017, the four Magnetospheric Multiscale spacecrafts were positioned within an electron diffusion region (EDR) just northward of a reconnection X line. The EDR was identified by electron crescent distributions, out-of-plane current, and energy conversion. From this position, the three spacecrafts closest to the X line (within about three electron inertial lengths) were able to accurately measure the reconnection electric field and the electron inflow velocity. The reconnection rates derived from the electric field and inflow velocity measurements agree with theoretical estimates (0.11–0.17) and a previous measurement of E_M in a tail reconnection event on 11 July 2017.

I. INTRODUCTION

Coupling of solar-wind energy into the Earth's magnetosphere occurs via magnetic reconnection, which creates open field lines that are swept into the geomagnetic tail. To complete the process, reconnection occurs again in the tail, thereby converting the open field lines to closed field lines, which convect toward the inner magnetosphere resulting in magnetospheric substorms and the aurora. Magnetic reconnection also plays a major energy-conversion role in solar physics, astrophysics, and laboratory plasma physics (Burch and Drake, 2009). The fundamental importance of magnetic reconnection for solar-wind magnetosphere interactions was the justification for the NASA Magnetospheric Multiscale (MMS) mission (Burch *et al.*, 2016a). One of the objectives of MMS is to determine the normalized reconnection rate or the inflow speed normalized by the outflow speed of reconnected field lines. The reconnection process occurs within an electron diffusion region (EDR), which surrounds an X line and within which electrons become demagnetized. Based on the time scales of solar and magnetospheric disturbances, Parker (1973) suggested a universal reconnection rate of at least 0.1 V_A, where V_A is the Alfvén speed in the upstream region, or a normalized reconnection rate of 0.1. Computer simulations leading up to the MMS launch in 2015 indicated that a reconnection rate of ~0.1 is a universal property of reconnection (Shay *et al.*, 1999), so tests of this conclusion became an important goal of the mission. Cassak *et al.* (2017) provide a historical view of how the maximum reconnection rate of 0.1 was derived from numerous experimental and theoretical studies and why it persists under a variety of assumptions from Hall MHD to resistive MHD to collisionless plasmas. With MMS, reconnection rates above 0.1 (up to 0.2) have been derived in the magnetotail (Genestreti *et al.*, 2018a) and in magnetosheath electron-only reconnection events (Burch *et al.*, 2020), while rates from 0.05 to 0.14 have been observed for magnetopause reconnection by Burch *et al.* (2020). It is now clear that there is not a universal rate or maximum rate of 0.1 and that much work is left to be done to determine what determines the actual rate.

There are at least three different ways of measuring the reconnection rate (Burch and Lewis, 1999): (1) measure the inflow velocity at the edge of the reconnection diffusion region, (2) measure the reconnection electric field, and (3) measure the aspect ratio of the diffusion region. These measurements require an accurate determination of the boundary-normal coordinate system with L along the reconnecting magnetic field, N normal to L in the plane of reconnection, and M along the reconnection X line. In these coordinates, the inflow velocity is $V_{\pm N}$; the reconnection electric field is E_{-M} at the magnetopause and E_M in the magnetotail, corresponding to a right-handed system; and the aspect ratio of the EDR is dL/dN.

As shown by Burch *et al.* (2020) for asymmetric magnetopause reconnection, when the inflow velocities at the edge of the EDR are scaled to the electron Alfvén speed (V_{Ae}), they provide reconnection rates (Karimabadi *et al.*, 2013; Klimas, 2015) because near the EDR, the magnetic field is advected by the electrons (Cassak *et al.*, 2005; Tsiklauri, 2008). This method of determining the reconnection rate has not been reported for tail reconnection, possibly because of the very low inflow velocities observed in the published events. For the tail reconnection event reported in this study, higher inflow velocities occurred, and this method is shown to be useful.

Methods (2) and (3) have been employed for the 11 July 2017 tail reconnection event by Genestreti *et al.* (2018a), Nakamura *et al.* (2018; 2019), and Torbert *et al.* (2018) with normalized reconnection rates between 0.1 and 0.2. For the 6 July 2017 event reported here, we have used data taken at times during which the four MMS spacecrafts were closely spaced at an average separation of about 17 km ($\sim$1.5 d_e) within a secondary EDR located within the exhaust region of a primary reconnection region. The EDR was identified by electron crescent distributions (Hesse *et al.*, 2014; Burch *et al.*, 2016b), out-of-plane current, and energy conversion seen simultaneously from all four spacecrafts. Because of the close spacing within the EDR, we were able to estimate fairly accurately the terms in the generalized Ohm's law with the result that the reconnection electric field was primarily formed by divergence of the electron pressure tensor. We used methods (1) and (2) to estimate the normalized reconnection rate. With method (1), the inflow velocity normalized to the electron Alfvén speed at the edge of the EDR gave reconnection rates between 0.11 and 0.14. With method (2), the reconnection electric field gave rates between 0.14 and 0.17 when normalized to the product of the ion Alfvén speed and reconnecting magnetic field in the tail lobe (as was done by Genestreti *et al.*, 2018a and Nakamura *et al.*, 2018).

II. OBSERVATIONS

A. Event identification

On 6 July 2017, MMS encountered a reconnecting current sheet in the geomagnetic tail. Orbit plots and the spacecraft (s/c) tetrahedron configuration are shown in Figs. 1 and 2, respectively. As shown in Fig. 1, the MMS constellation, denoted by the cyan diamond, was northward of the neutral sheet at a geocentric distance of about 22 R_E. Although not shown, MMS was located in the pre-midnight region at about 2300 MLT (magnetic local time). Figure 2 shows the spatial configuration of the four s/c, which had an average separation of $\sim$17 km, one of the smallest used to date in the tail region. While this small

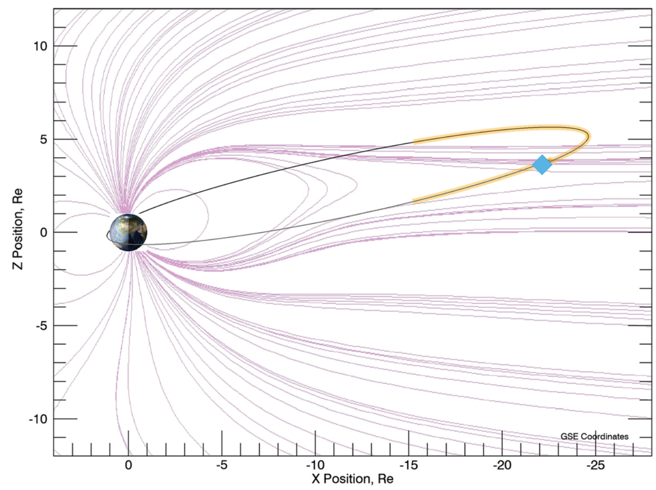

FIG. 1. MMS orbit on 6 July 2017 in geocentric solar ecliptic (GSE) coordinates. The MMS position is marked by the cyan diamond, which in GSE was X = 1.410 R_E, Y = 1.417 R_E, and Z = 2.318 R_E. The science region of interest (SROI) for this orbit is shown in gold over which burst-mode data were acquired. Magnetic field lines are from a magnetic field model using parameters from OMNI (Operating Missions as a Node on the Internet) (King and Papitashvili, 2004): ram pressure, 2.14 nPa, IMF By, −4.6 nT, IMF Bz, −0.2 nT.

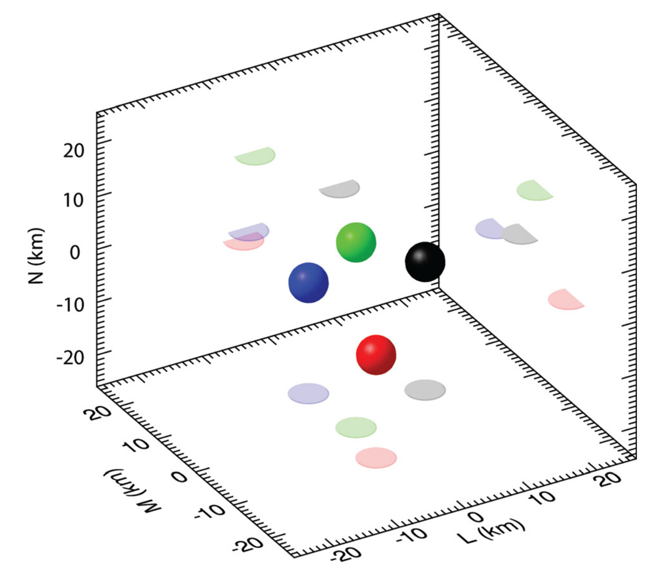

FIG. 2. Spacecraft tetrahedron: MMS1 black, MMS2 red, MMS3 green, and MMS4 blue. The GSE components of the boundary normal coordinates are L = [0.9933, −0.0195, −0.1139], M = [−0.0092, 0.9692, −0.2461], and N = [0.1152, 0.2455, 0.9625], which were derived using the method of Denton *et al.* (2018) in which L is the maximum variance direction of *B* (MVAB) and N is the direction of maximum directional derivative of *B*.

separation perhaps prevented the s/c from sampling both sides of the X line, it did allow for simultaneous four-point measurements of inflow velocities and reconnection electric fields in the EDR.

A 12-s summary plot of MMS2 data on 6 July 2017 is shown in Fig. 3 where the EDR event of interest is bracketed by the two maroon-colored vertical lines. As shown in Figs. 3(a) and 3(b), the L component of *B* was positive throughout the interval, indicating that the spacecraft was north of the neutral sheet. Two near magnetic nulls occurred just before the EDR was encountered. Also notable is that the ion velocity was positive (earthward) throughout the interval, indicating that the EDR was part of a secondary reconnection site located in the earthward exhaust of a primary reconnection site tailward of the MMS constellation. The most prominent feature shown in Figs. 3(g) and 3(h) is the peak of electron velocity in the −M direction and the associated current in the M direction. This feature is the reconnection out-of-plane current, which, along with significant $J_M E_M$ [Fig. 3(l)] and electron crescent distributions (shown later), strongly indicates the encounter with an EDR. Between the EDR and the vertical blue line labeled "lobe," MMS2 passed through a turbulent region, which we identify as the plasma-sheet boundary layer (PSBL), until it emerged into the lobe. Although there is energy dissipation ($J E$) and strong wave activity in the PSBL, there are no indications of EDRs.

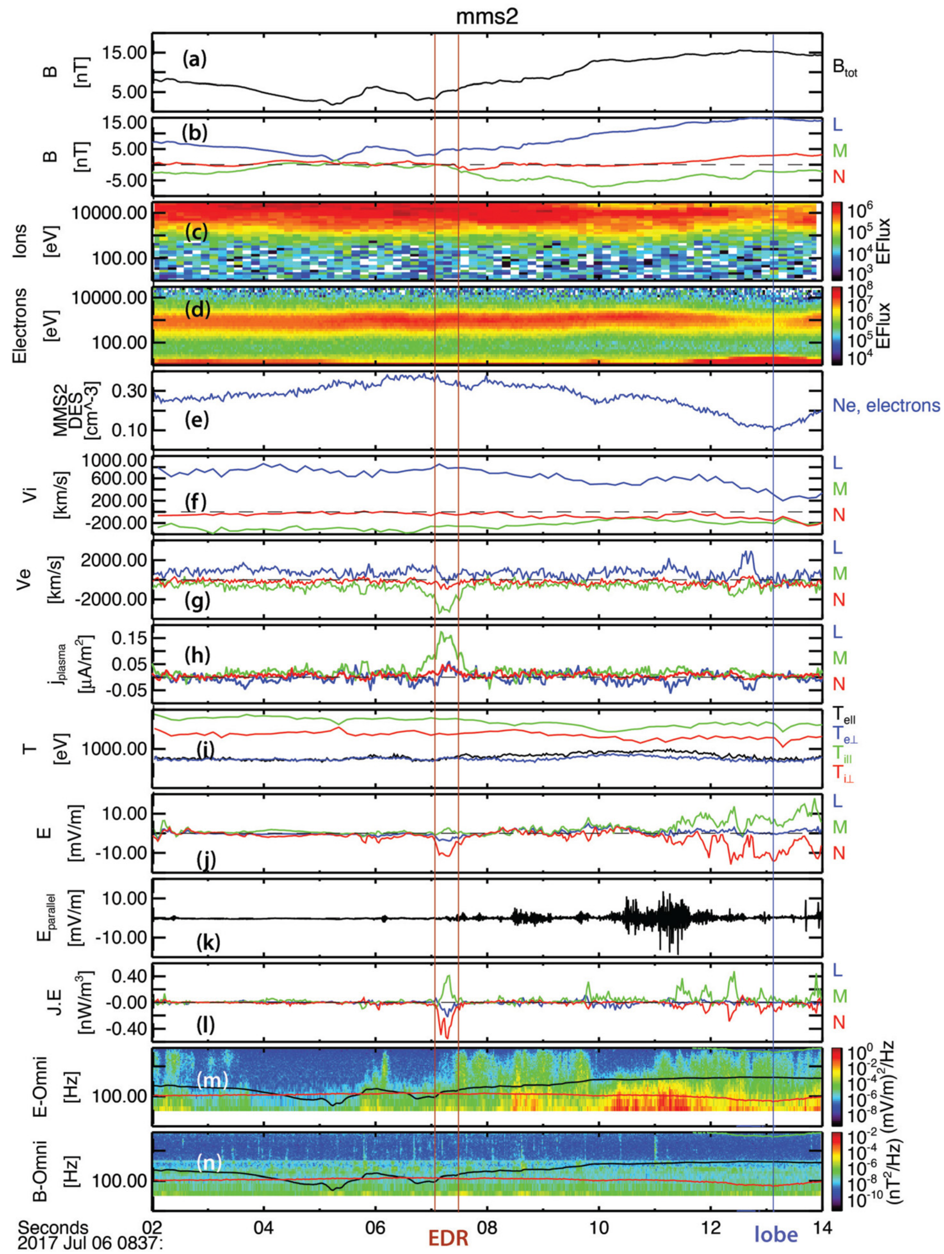

FIG. 3. MMS2 measurements on 6 July 2017. (a) B magnitude, (b) vector *B*, (c) ion energy/charge vs time with energy flux (EFlux) in units of eV cm^{-2} sr^{-1} s^{-1} eV^{-1}, (d) electron energy vs time, (e) electron density, (f) ion velocity, (g) electron velocity, (h) current derived from plasma measurements, (i) ion and electron temperature, (j) vector *E*, (k) parallel *E*, (l) *J*·*E* ($J_L E_L$ in blue, $J_M E_M$ in green, $J_N E_N$ in red), (m) E power spectrum, and (n) B power spectrum. EDR event of interest is bounded by the two maroon-colored vertical lines. The vertical blue line indicates a spacecraft encounter with the edge of the tail lobe at which the electron density and magnetic field strength are used to compute the upstream electric field for the calculation of the reconnection rate.

The magnetic field strength and plasma density in the lobe are used in Sec. III B to determine the electric field in the large-scale inflow region of reconnection.

B. Comparison to simulation

In order to identify the context of the observed reconnecting current sheet within the larger region of tail reconnection, we performed a simulation of the type described by Hesse *et al.* (2018) for the conditions encountered in our event with the results shown in Fig. 4. The 2.5-dimensional particle-in-cell (PIC) simulation starts from a Harris sheet with an additional density of 0.2 and a small, X-type perturbation. While periodic boundary conditions are used in the simulation, the resulting recirculating flows do not reach the region of interest during the simulation run. The top panel of Fig. 4 shows the out-of-plane (y component) current density with a primary X line apparent at about 50 d_i ($di = c/\omega_{pi}$, the ion inertial length within the Harris sheet) and secondary X lines to the left and right of it. The secondary X line that we identify with our region of interest is the one on the Earthward (right-hand) side of the primary X line between 60 and 70 d_i. In the bottom panel, Fig. 4 is plotted B_z, v_{ix}, and v_{ex} along $z = 0$, and the most prominent feature being the large electron jet reversal at the primary X line. A smaller electron jet reversal shifted toward positive v_{ex} occurs at the secondary X line, noted by the horizontal blue bar. The ion velocity, v_{ix}, remains positive across the secondary X line, which is consistent with it being located in the exhaust of a primary X line. Reference to Figs. 3(f) and 3(g) shows that the same pattern of v_{ix} and $v_{ex,}$ (blue traces) occurred at the EDR region denoted by the two maroon-colored vertical lines. A closer look at these ion and electron velocities is shown later.

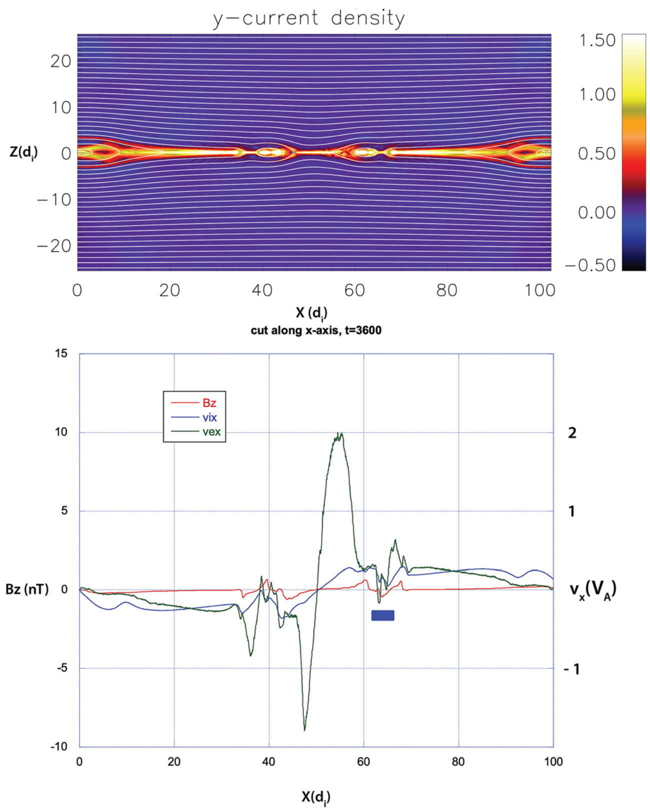

FIG. 4. Top: Current density in 2.5D simulation with proton/electron mass ratio = 100; dimensions of $L_x = 102.4\ c/\omega_{pi}$, $L_z = 51.2\ c/\omega_{pi}$; 3200 × 3200 grid; 7 × 10^{10} particles; and $T_e/T_i = 0.2$. *Bottom*: Plot along z = 0 of B_Z (red), v_{ix} (blue), and v_{ex} (green). V_A is the ion Alfvén speed. The blue rectangle shows the estimated location of the event of interest in this study as noted in Fig. 3. Periodic boundary conditions are used in the simulation.

C. X line reconstruction

In order to determine the configuration of magnetic field lines in the vicinity of the X line, we used the method of Torbert *et al.* (2020) and Denton *et al.* (2020). The method of Denton *et al.* (2020) was used to obtain the results shown in Figs. 5 and 6. Shown in Fig. 5 is a red square with a dimension of 50 km, which is ~5 d_e or 3.3 r_g for a 500-eV electron, where d_e is the electron inertial length (c/ω_{pe}) and r_g is the electron gyro-radius. Figure 5 shows that the four MMS spacecraft were all located northward of the X line within about 4 d_e or 2.5 r_g of the X line.

Figure 6 shows the temporal development of the X line reconstruction at 0.03s intervals from 08:37:07.05 to 08:37:07.30 UT. The sequence of plots from 08:37:07.05 to 08:37:07.3 UT shows a movement of the X line toward the left, which is the tailward direction, of about 260 km/s as compared to the earthward ion flow of about 700 km/s shown in Fig. 3(f).

D. Generalized Ohm's law analysis

Evaluation of the generalized Ohm's law for dayside reconnection events sampled with MMS has been performed by Torbert *et al.* (2016) and Genestreti *et al.* (2018b). Since the average spacecraft

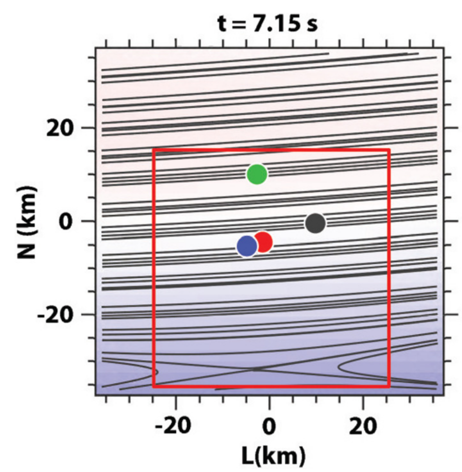

FIG. 5. Two-dimensional cut through 3D reconstructions of the magnetic field on 6 July 2017 at 08:37:07.14 UT using a polynomial method (Denton *et al.*, 2020) with dimensions in km, where the red square has dimensions 5 d_e (electron diffusion length) and 3.3 r_g (500 eV electron gyroradius). The four spacecraft are shown by symbols in black, red, green, and blue for MMS1, 2, 3, and 4. The color shading indicates B_M with red shades showing positive values and blue shades showing negative values.

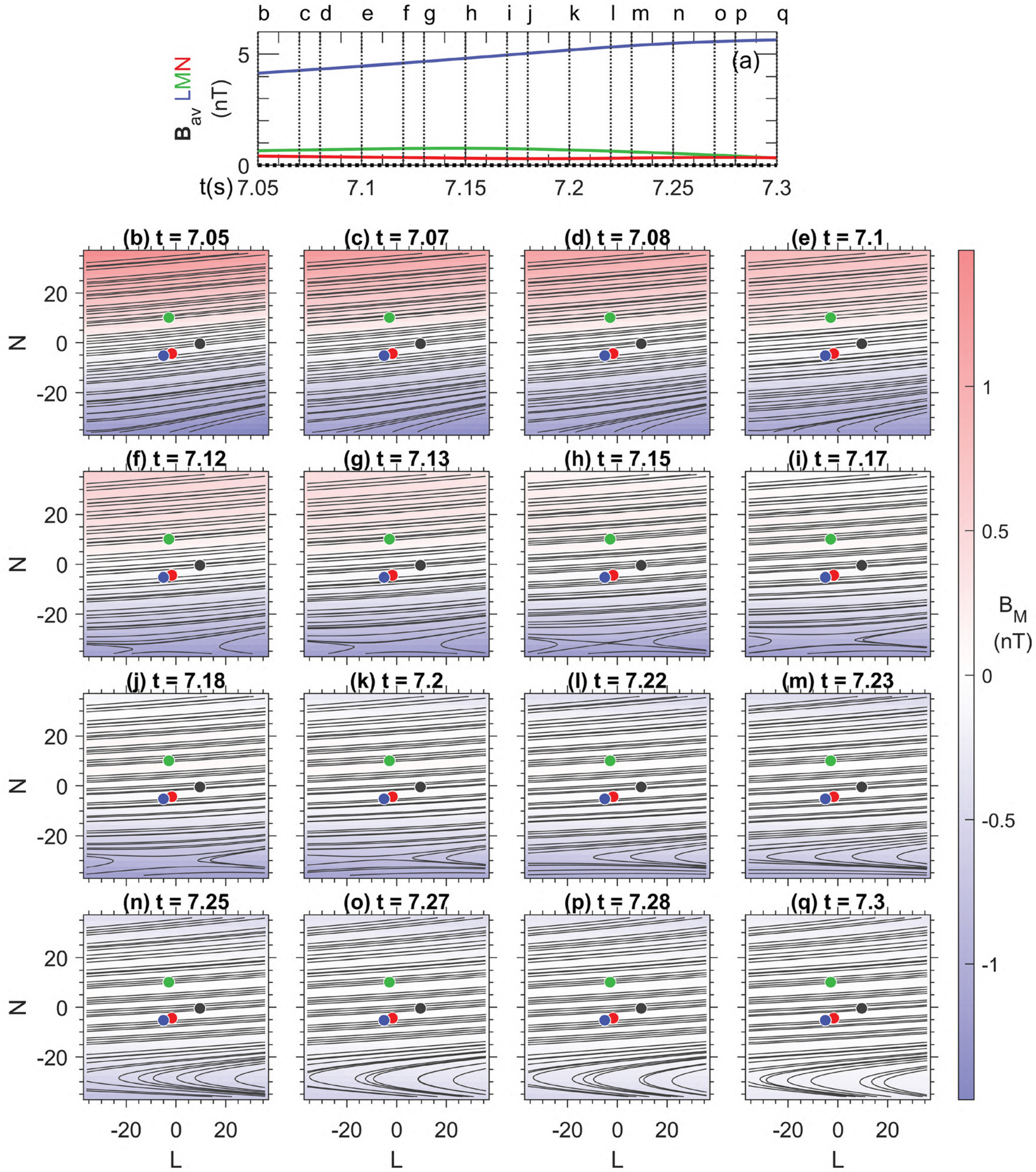

FIG. 6. Time history of reconstruction of X-line on 6 July 2017. The top panel (a) shows the magnetic field at the barycenter of the four spacecraft. The spacecraft locations in the bottom 16 panels are shown by diamonds with MMS1, 2, 3, and 4 in black, red, green, and blue, respectively. The sequence of plots from 08:37:07.05 to 08:37:07.3 UT shows a movement of the X line toward the left, which is the tailward direction.

separation of ∼17 km for this event was much smaller than the typical separation of ∼40 km in the magnetotail, it is expected that the sources of the reconnection electric field could be determined more accurately than for other tail events because all four spacecraft were simultaneously located within the EDR. For the analysis of the 6 November 2017 event, we followed the approach of Genestreti *et al.* (2018a) by computing the barycentric current with curl*B* from the four MMS spacecraft and determining the electric field resulting from the FPI measurements of the divergence of the electron pressure tensor ($-\nabla\cdot\bar{P}_e/en$) and the inertial electric field $[-m_e\nabla\cdot(v_e v_e)/en]$. Figure 7 shows the total $J\cdot E'$ in black, $J\cdot E'$ from the inertial electric field at the barycenter of the four spacecraft ($J\cdot E'_{\mathrm{Inertial}}$) in blue and $J\cdot E'$ from the

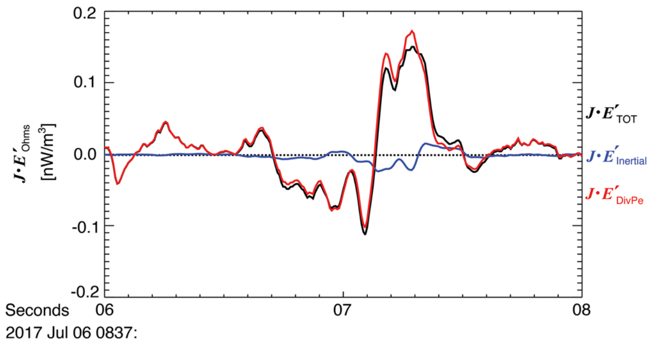

FIG. 7. Evaluation of the contribution of the inertial term, E'_{Inertial}, and the divergence of the pressure tensor term, E'_{DivPe}, to the total $J{\cdot}E'_{\mathrm{Ohms}}$, where E' is the electric field in the rest frame of the electrons [$E' = E + (v_e \times B)$]. The plots show $J{\cdot}E'_{TOT}$ in black, $J{\cdot}E'_{\mathrm{Inertial}}$ in blue, and $J{\cdot}E'_{\mathrm{DivPe}}$ in red. Components were determined from all four MMS spacecraft with J determined from curl$B$ and E' determined from the average electric field of the four spacecraft at their barycenter.

divergence of the electron pressure tensor at the barycenter ($J{\cdot}E'_{\mathrm{DivPe}}$) in red. We note that the total $J{\cdot}E'$ compares favorably with that shown for MMS2 in Fig. 3. The inertial term is very small, while the pressure divergence term is larger by almost a factor of ten. Between 7.18 s and 7.28 s, $J{\cdot}E'$ is positive.

E. Plasma conditions within the electron diffusion region

Shown in Fig. 8 is the measured electron velocities and electric fields for all four spacecraft as they passed through the EDR, which is bounded by maroon vertical lines. Also shown in Figs. 8(a)–8(c) is the ion velocity averaged over the four s/c (dashed magenta curves).

Within the EDR, the MMS3 M and N components of electric fields and electron velocities deviated significantly from those of the other three s/c, which agreed fairly closely with each other. Again, this difference is attributed to the fact that MMS3 was about twice as far north of the X line than the other three s/c. Figure 8(a) shows that both v_{eL} and v_{iL} remained positive before the EDR encounter, which is consistent with the flow from a primary X line located tailward of the MMS position. However, as shown in Fig. 8(a), v_{eL} dropped to near zero within the EDR as the flow turned toward the X line, with v_{eN} becoming negative in Fig. 8(c). Figure 8(b) shows the out-of-plane electron velocity, which reached negative values greater than 3000 km/s for MMS 1, 2, and 4 with somewhat lower values for MMS3, while v_{iM} maintained a negative value of only a few hundred km. Figure 8(c) shows v_{eN}, the inflow velocity, which was negative (southward) and peaked strongly in the latter part of the EDR (between 07.2 and 07.3 s). Again, the traces are very similar for MMS 1, 2, and 4 with a significant difference for MMS3. Figures 8(d)–8(f) shows the electric field measurements with small values along L, peak values along M in the same time 07.2–07.3 s time period noted for the inflow velocity, and strong negative values along N (the Hall electric field). Because of the peaks in v_{eM} and E_M, we identify the time period 07.2–07.3 s as the inner EDR and will use this time period to derive reconnection rates in sections that follow.

Figure 9 provides field and plasma data from all four MMS spacecraft during the EDR encounter. We note first, as in Fig. 8, the strong similarity of all parameters for MMS1, 2, and 4 with some notable differences for MMS3, because of its position farther from the X line. For the line plots in Figs. 9(a)–9(e), the vertical dashed lines indicate the EDR. Figure 9(a) shows the magnetic field components in the LMN coordinate system shown in the caption of Fig. 2. Figure 9(b) shows the electron bulk velocity with the L component decreasing to small values within the EDR as noted in Fig. 8(a), the M component being most prominent and accounting for the out-of-plane current, and the N component having small negative values as expected for the reconnection inflow velocity. Figure 9(c) shows small L components of E, somewhat larger positive values of E_M (the reconnection E field), and the largest component, E_N, as the Hall electric field. Figure 9(d) contains $J_M{\cdot}E_M'$, showing that the energy conversion associated with the out-of-plane components of J and E' is tightly constrained within the EDR for MMS1, 2, and 4 but with a profile for MMS3 that is broadened and shifted toward earlier times.

Figures 9(f)–9(h) show reduced electron velocity distribution functions (VDFs) for MMS 1, 2, and 4, summed over the axis orthogonal to each displayed pane and measured within the EDR every 30 ms after 08:37:07 UT as noted by the red numbers in each frame, which denote the start time of each VDF. The VDFs [panels (f)–(h)] are plotted in the $v_{\perp 1}$–$v_{\perp 2}$ plane and show crescent distributions along the $v_{\perp 1}$ axis.

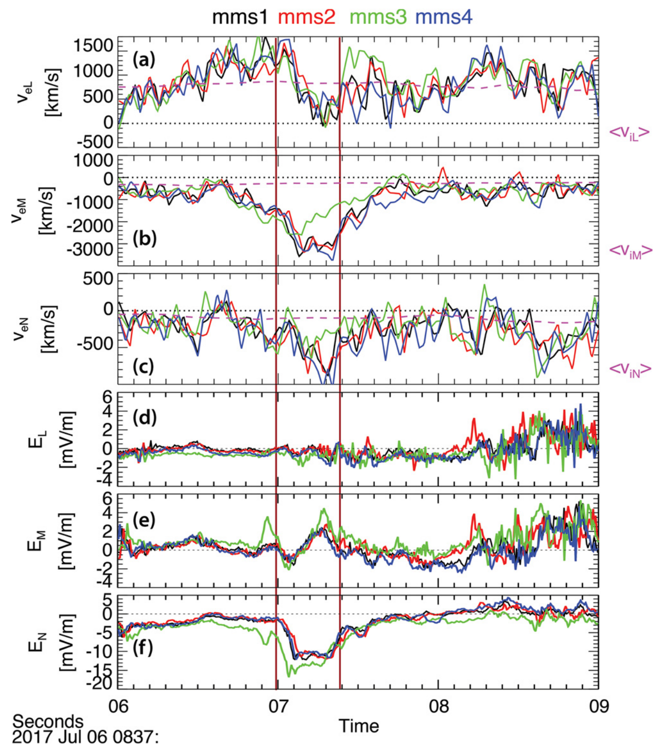

FIG. 8. Electron velocities and electric fields for MMS1-4 on 6 July 2017. (a) v_{eL} for each spacecraft along with v_{iL} averaged over all four spacecraft (magenta curve). (b) Same as (a) except for the M component. (c) Same as (a) except for the N component. (d)–(f) E_L, E_M, and E_N for each spacecraft. Vertical maroon lines show the EDR region of interest.

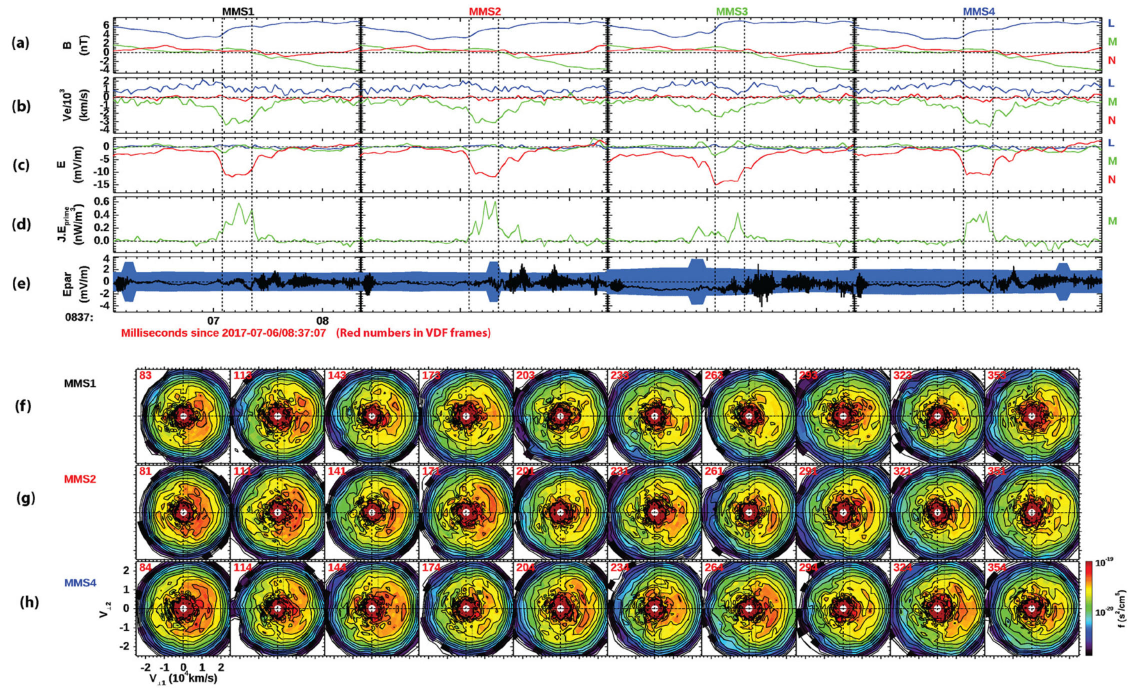

FIG. 9. Plasma and field data from MMS1-4 on 6 July 2017. (a) Magnetic field components (LMN). (b) Electron velocity in units of 10^3 km/s. (c) Electric field. (d) M component of $J\cdot E'$. (e) Parallel electric field with the error band in blue. (f)–(h) Reduced electron velocity distribution functions (summed over $v_{||}$) in the $v_{\perp 1}$–$v_{\perp 2}$ plane with $v_{\perp 1}$ in the $(b \times v) \times b$ direction, which is a proxy for $E \times B$ and $v_{\perp 2}$ in the E direction for MMS1, 2, and 4. Red numbers within each frame of (f)–(h) show the start time of each VDF in milliseconds after 08:37:07 UT.

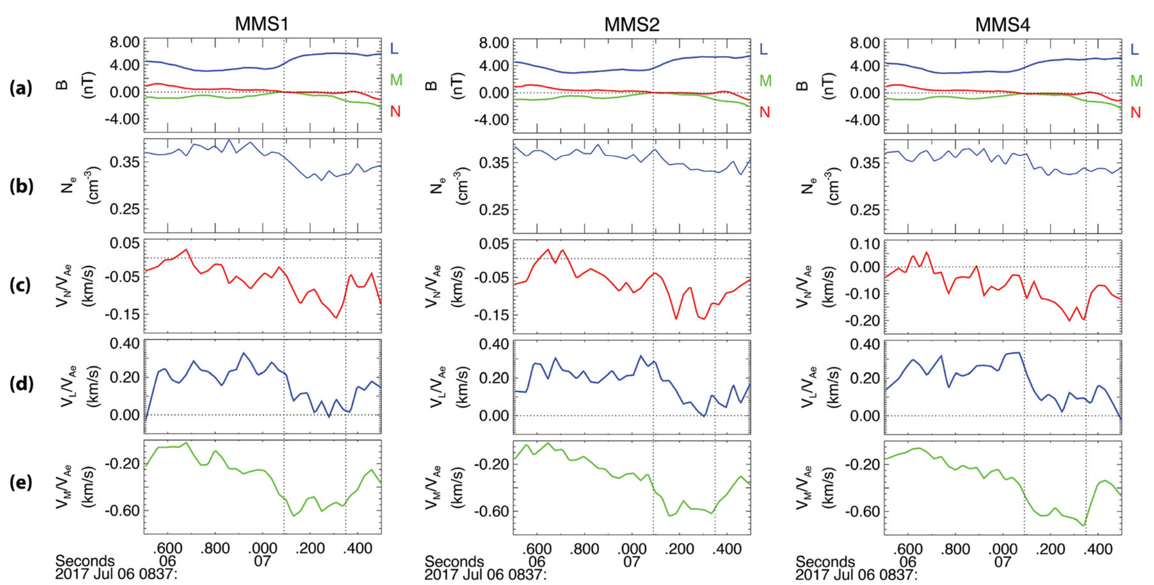

FIG. 10. Plasma and field parameters on 6 July 2017 with vertical dotted lines marking the approximate edges of the EDR for MMS1, 2, and 4. (a) Magnetic field LMN components. (b) Electron density. (c) v_{eL}/v_{AeL}. (d) v_{eM}/v_{AeL}. (e) v_{eN}/v_{AeL}, where v_{AeL} is the mean electron Alfvén speed with $B = B_L$ for each spacecraft over the first half of each plot (08:37:06.5–08:37:07.0 UT), which is an estimate of the inflow speed at the edge of the EDR. The v_{AeL} values for MMS1-4 are 5519, 5289, 6141, and 5223 km/s, respectively. For comparison, the structure velocity along N, as determined from Figs. 2, 6, and 8 is ~40–50 km/s and so is of negligible importance and is, hence, disregarded. The minimum values of v_N/v_{AeL}, which is the normalized reconnection rate, are 0.16 for MMS1, 0.16 for MMS2, and 0.20 for MMS4. For comparison, the mean values of v_{eN}/v_{AeL} within the entire EDR (08:37:07.09–08:37:07.35 UT) are 0.11, 0.11, and 0.14 for MMS1, 2, and 4, respectively.

III. DETERMINATIONS OF RECONNECTION RATE

A. Using electron inflow velocity

Figure 10 shows (a) the magnetic-field LMN components, (b) electron density, (c) electron inflow velocity (N direction), (d) outflow velocity from primary X line (L direction), and (e) out-of-plane electron velocity (M direction). All velocities are normalized to the electron Alfvén speed. As used by Burch *et al.* (2020) for a dayside magnetopause reconnection event, the normalized inflow velocity gives the normalized reconnection rate. For MMS 1, 2, and 4, the minimum value of v_{eN}/v_{eA} was between 0.15 and 0.2 and was located within the region of strong out-of-plane velocity, v_{eM}/v_{eA}, which is the best measure of closest approach to the X line.

B. Using reconnection electric field

Another measurement of the reconnection rate is the reconnection electric field, E_M, with the normalized reconnection rate being E_M/E_o, where E_o is the convection electric field of the inflow. One approach to obtaining E_o is determining the reconnecting magnetic field (B_L) and the ion Alfvén speed in the lobe region so that $E_o = v_{iAL}B_L$, as was done by Nakamura *et al.* (2018) and Genestreti *et al.* (2018a) for another magnetotail reconnection event. Another approach is to evaluate E_o at the edge of the EDR with $E_o = v_{eAL}B_L$, as was done by Burch *et al.* (2020) for a magnetopause reconnection event. We used both approaches after determining E_M in the EDR by eliminating contamination from E_N, as described by Genestreti *et al.* (2018a), and also from E_L.

Figure 11 shows magnetic and electric fields from MMS1 and MMS4 for the time period 08:37:06.8–07.4 UT on 6 July 2017. Figures 10(a)–10(d) shows the LMN components using the transformation in the caption of Fig. 2. As noted by Genestreti *et al.* (2018a), E_M is normally the smallest electric-field component, particularly when compared to E_N and so is subject to contamination from the other two components. While Genestreti *et al.* (2018a) tested numerous different coordinate transforms to find an optimum one with minimal contamination from E_N, we started with the transformation used up until now and used trial and error to minimize the contamination as was done by Burch *et al.* (2020) for a magnetopause reconnection event. The new transform, $L^*M^*N^*$, is shown in the caption of Fig. 11. As shown in Figs. 11(e) and 11(f), the E_M analysis was performed over the zoomed-in time interval 7.21–7.29 s where E_M remained positive. That the same time interval and the same $L^*M^*N^*$ coordinate transform applied to

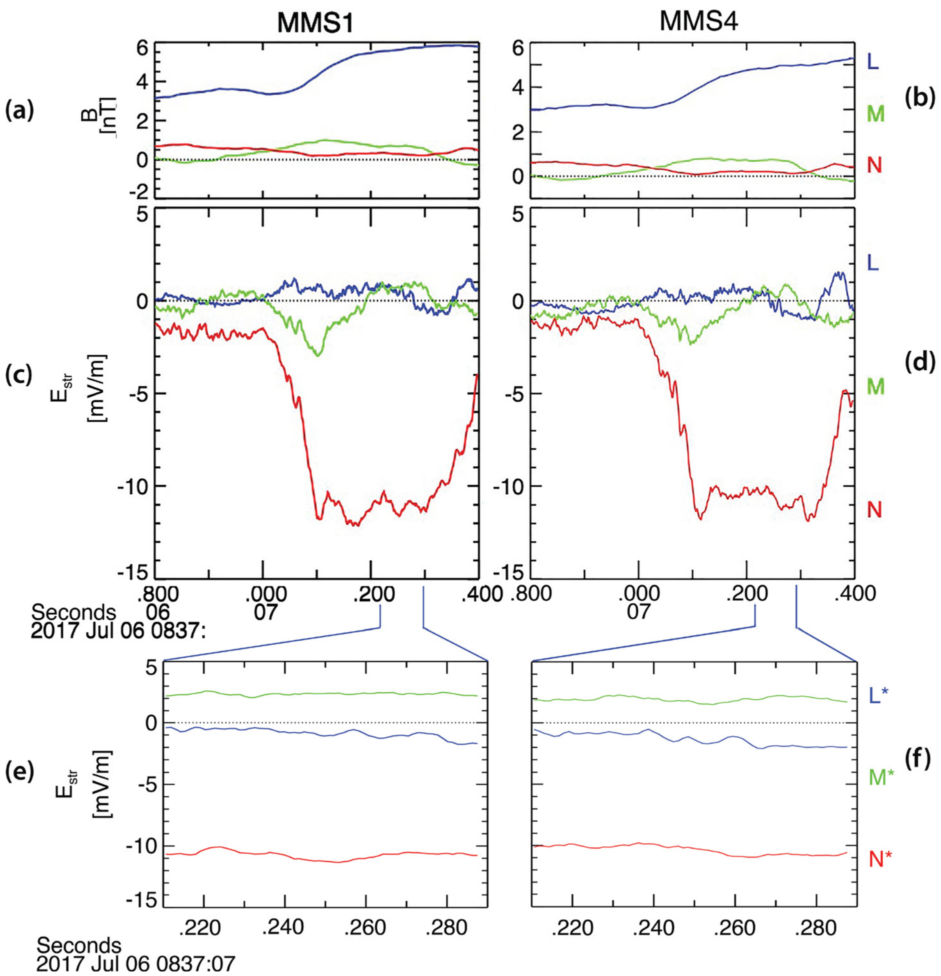

FIG. 11. Magnetic and electric fields within an EDR on 6 July 2017. (a) and (b) Magnetic field components from MMS1 and MMS4. (c) and (d) Electric field in the structure frame from MMS1 and MMS4. (e) and (f) Electric field components in the structure frame from MMS1, MMS4 with modified LMN transformation from GSE: $L^* = [0.974\,719\,58, -0.218\,937\,99, 0.045\,142\,658]$, $M^* = [0.218\,700\,08, 0.891\,853\,21, -0.395\,898\,31]$, and $N^* = [0.046\,388\,421, 0.395\,668\,57, 0.917\,159\,56]$.

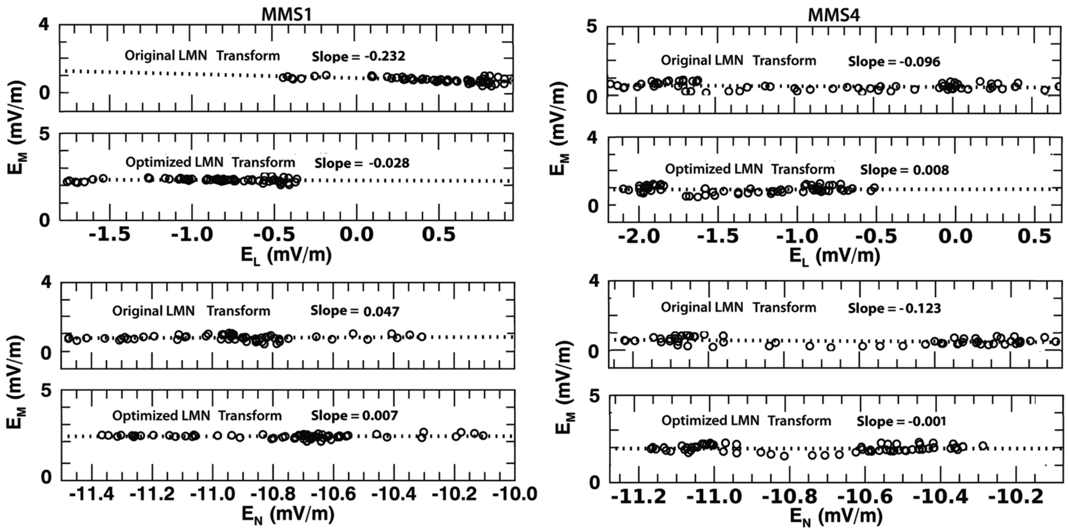

FIG. 12. Plots of E_M vs E_L and E_M vs E_N for MMS1 (left) and MMS4 (right) for 08:37:07.210–07.290 on 6 July 2017. For each pair of plots, the top one is for the original LMN transform shown in the Fig. 2 caption, and the bottom one is for the modified LMN transform shown in the Fig. 11 caption. The slopes of the linear fits are shown in each panel. In each case, the optimized transform results in a nearly horizontal line fit, indicating essentially no dependence of E_M on either E_L or E_N with the absolute values of all slopes less than 0.03. For MMS1, $E_M = 2.00$ mV/m for the original LMN transform and $E_M = 2.35$ mV/m for the optimized LMN transform. Corresponding values for MMS4 are 1.86 and 1.94 mV/m, respectively. Standard deviations of the optimized E_M are 0.10 mV/m for MMS1 and 0.20 mV/m for MMS4.

both MMS1 and MMS4 are consistent with their near co-location in the L–N plane and separation of about 20 km along M (parallel to the X line).

Figure 12 shows scatterplots of E_M vs E_L and E_M vs E_N for MMS1 and MMS4 for the original LMN transform and the optimized $L^*M^*N^*$ transform. Noted in Fig. 12 caption is the original average of E_M and its optimized value, which for MMS1 was 2.35 mV/m and for MMS4 was 1.94 mV/m. Referring to Fig. 3, where the lobe encounter of MMS2 is noted by the vertical blue line, we find that $E_o = v_{iA}B_L = 14.1$ mV/m. Using this value, the normalized reconnection rates for MMS1 and MMS4 were 0.17 and 0.14, respectively. The alternate approach, using $E_o = v_{eA}B_L$ in the EDR inflow region, gives $E_o = 38.2$ mV/m and normalized reconnection rates for MMS1 and MMS4 of 0.06 and 0.05, respectively. While both approaches give results within a factor of two of 0.1, the significant differences are not unexpected because of different inflow regimes of the lobe and the EDR inflow region. The fact that using the inflow velocity yielded normalized reconnection rates intermediate between the rates determined by the two E_M methods is perhaps evidence that all three methods are valid considering the uncertainties in both the geometry of the X-line structure and the depth of penetration of MMS into the tail lobe.

IV. SUMMARY AND CONCLUSIONS

A unique configuration of MMS spacecraft in the tail region on 6 July 2017 was investigated in this study. The event was unique because the average s/c separation was small ($\sim$17 km), and the X line, which was located within the Earthward exhaust of a primary X line, was moving tailward at about 260 km/s.

The normalized reconnection rate was determined by two different methods, electron inflow velocity and reconnection electric field, with results in the range of theoretical prediction. First, by measuring the electron inflow velocity (v_{eN}) for the first time in a tail reconnection event, we found, after normalizing the inflow velocity to the product of the electron Alfvén speed and the reconnecting magnetic reconnection rates between 0.16 and 0.2 for the four spacecraft. Second, the reconnection electric field (E_M) was measured accurately by eliminating contamination from the L and N components with an optimized boundary normal coordinate (LMN) transform. When E_M was normalized to the lobe inflow velocity estimate ($v_{iA}B_L$), reconnection rates for MMS1 and MMS4, which were closest to the X line, were found to be 0.17 and 0.14, respectively, in good agreement with the values determined by the electron inflow velocity. When, alternatively, E_M was normalized to $v_{eA}B_L$ in the inflow region, lower reconnection rates of 0.06 and 0.05 were found. Further refinement of these rates should be possible through analysis of other events.

ACKNOWLEDGMENTS

This work was supported by NASA under Contract No. NNG04EB99C at SwRI (Southwest Research Institute). The OMNI data were obtained from the Goddard Space Flight Center/SPDF (Space Physics Data Facility) OMNIWeb interface at https://omniweb.gsfc.nasa.gov.

AUTHOR DECLARATIONS

Conflict of Interest

The authors have no conflicts to disclose.

DATA AVAILABILITY

The entire MMS dataset is available online at https://lasp.colorado.edu/mms/sdc/public/links/. Fully calibrated data are placed online at this site within 30 days of their transmission to the MMS Science Operations Center. The data are archived in the NASA Common Data

Format (CDF) and can be plotted using a number of different data display software packages that can use CDF files. A very comprehensive system called the Space Physics Environment Data Analysis System (SPEDAS) is available by downloading http://themis.ssl.berkeley.edu/socware/bleeding_edge/ and selecting spdsw_latest.zip. Training sessions on the use of SPEDAS are held on a regular basis at space physics related scientific meetings. All of the data plots in this paper were generated with SPEDAS software applied to the publicly available MMS database, so they can readily be duplicated (see MMS Science Data Center).

REFERENCES

Burch, J. L. and Drake, J. F., "Reconnecting magnetic fields," Am. Sci. **97**, 392–399 (2009).

Burch, J. L. and Lewis, W. S., "Science objectives of the Magnetospheric Multiscale mission: The microphysics of reconnection," in *Physics of Space Plasmas*, edited by T. Chang and J. R. Jasperse (MIT Center for Theoretical Geo/Cosmo Plasma Physics, 1999).

Burch, J. L., Moore, T. E., Torbert, R. B., and Giles, B. L., "Magnetospheric Multiscale overview and science objectives," Space Sci. Rev. **199**, 5–21 (2016a).

Burch, J. L., Torbert, R. B., Phan, T. D., Chen, L.-J., Moore, T. E., Ergun, R. E., Eastwood, J. P., Gershman, D. J., Cassak, P. A., Argall, M. R., Wang, S., Hesse, M., Pollock, C. J., Giles, B. L., Nakamura, R., Mauk, B. H., Fuselier, S. A., Russell, C. T., Strangeway, R. J., Drake, J. F., Shay, M. A., Khotyaintsev, Y. V., Lindqvist, P.-A., Marklund, G., Wilder, F. D., Young, D. T., Torkar, K., Goldstein, J., Dorelli, J. C., Avanov, L. A., Oka, M., Baker, D. N., Jaynes, A. N., Goodrich, K. A., Cohen, I. J., Turner, D. L., Fennell, J. F., Blake, J. B., Clemmons, J., Goldman, M., Newman, D., Petrinec, S. M., Trattner, K. J., Lavraud, B., Reiff, P. H., Baumjohann, W., Magnes, W., Steller, M., Lewis, W., Saito, Y., Coffey, V., and Chandler, M., "Electron-scale measurements of magnetic reconnection in space," Science **352**, aaf2939 (2016b).

Burch, J. L., Webster, J. M., Hesse, M., Genestreti, K. J., Denton, R. E., Phan, T. D., Hasegawa, H., Cassak, P. A., Torbert, R. B., Giles, B. L., Gershman, D. J., Ergun, R. E., Russell, C. T., Strangeway, R. J., Le Contel, O., Pritchard, K. R., Marshall, A. T., Hwang, K.-J., Dokgo, K., Fuselier, S. A., Chen, L.-J., Yamada, M., Wang, S., Swisdak, M., Drake, J. F., Argall, M. R., Trattner, K. J., and Paschmann, G., "Electron inflow velocities and reconnection rates at Earth's magnetopause and magnetosheath," Geophys. Res. Lett. **47**, e2020GL089082, https://doi.org/10.1029/2020GL089082 (2020).

Cassak, P. A., Liu, Y.-H., and Shay, M. A., "A review of the 0.1 reconnection rate problem," J. Plasma Phys. **83**, 715830501 (2017).

Cassak, P. A., Shay, M. A., and Drake, J. F., "Catastrophe model for fast magnetic reconnection onset," Phys. Rev. Lett. **95**(23), 235002 (2005).

Denton, R. E., Sonnerup, B. U. Ö., Russell, C. T., Hasegawa, H., Phan, T. D., Strangeway, R. J., Giles, B. L., Ergun, R. E., Lindqvist, P.-A., Torbert, R. B., Burch, J. L., and Vines, S. K., "Determining *L–M–N* current sheet coordinates at the magnetopause from Magnetospheric Multiscale data," J. Geophys. Res.: Space Phys. **123**, 2274–2295, https://doi.org/10.1002/2017JA024619 (2018).

Denton, R. E., Torbert, R. B., Hasegawa, H., Dors, I., Genestreti, K. J., Argall, M. R., Gershman, D., Le Contel, O., Burch, J. L., Russell, C. T., Strangeway, R. J., Giles, B. L., and Fischer, D., "Polynomial reconstruction of the reconnection magnetic field observed by multiple spacecraft," J. Geophys. Res.: Space Phys. **125**, e2019JA027481, https://doi.org/10.1029/2019JA027481 (2020).

Genestreti, K. J., Nakamura, T. K. M., Nakamura, R., Denton, R. E., Torbert, R. B., Burch, J. L., Plaschke, F., Fuselier, S. A., Ergun, R. E., Giles, B. L., Torbert, R. B., and Russell, C. T., "How accurately can we measure the reconnection rate for the MMS diffusion region event of 11 July 2017?," J. Geophys. Res.: Space Phys. **123**(11), 9130–9149, https://doi.org/10.1029/2018JA025711 (2018a).

Genestreti, K. J., Varsani, A., Burch, J. L., Cassak, P. A., Torbert, R. B., Nakamura, R., Ergun, R. E., Giles, B. L., Russell, C. T., Escoubet, C. P., Fear, R. C., and Baumjohann, W., "MMS observation of asymmetric reconnection supported by 3-D electron pressure divergence," J. Geophys. Res: Space Phys. **123**, 1806–1821, https://doi.org/10.1002/2017JA025019 (2018b).

Hesse, M., Aunai, N., Sibeck, D., and Birn, J., "On the electron diffusion region in planar, asymmetric, systems," Geophys. Res. Lett. **41**, 8673–8680, https://doi.org/10.1002/2014GL061586 (2014).

Hesse, M., Norgren, C., Tenfjord, P., Burch, J. L., Liu, Y.-H., Chen, L.-J., Bessho, N., Wang, S., Nakamura, R., Eastwood, J. P., Hoshino, M., Torbert, R. B., and Ergun, R. E., "On the role of separatrix instabilities in heating the reconnection outflow region," Phys. Plasmas **25**, 122902 (2018).

Karimabadi, H., Roytershteyn, V., Daughton, W., and Liu, Y.-H., "Recent evolution in the theory of magnetic reconnection and its connection with turbulence," Space Sci. Rev. **178**(2–4), 307–323 (2013).

King, J. H. and Papitashvili, N. E., "Solar wind spatial scales in and comparisons of hourly Wind and ACE plasma and magnetic field data," J. Geophys. Res.: Space Phys. **110**(A2), A02104, https://doi.org/10.1029/2004JA010649 (2005).

Klimas, A., "New expression for collisionless magnetic reconnection rate," Phys. Plasmas **22**(4), 042901 (2015).

MMS Science Data Center, see https://lasp.colorado.edu/mms/sdc/public/ for "MMS Science Data Center—The official data archive of the MMS mission. Contains data, plots, and other useful information relevant to MMS."

Nakamura, R., Genestreti, K. J., Nakamura, T., Baumjohann, W., Varsani, A., Nagai, T., Bessho, N., Burch, J. L., Denton, R. E., Eastwood, J. P., Ergun, R. E., Gershman, D. J., Giles, B. L., Hasegawa, H., Hesse, M., Lindqvist, P.-A., Russell, C. T., Stawarz, J. E., Strangeway, R. J., and Torbert, R. B., "Structure of the current sheet in the 11 July 2017 electron diffusion region event," J. Geophys. Res.: Space Phys. **124**(2), 1173–1186, https://doi.org/10.1029/2018JA026028 (2019).

Nakamura, T. K. M., Genestreti, K. J., Liu, Y.-H., Nakamura, R., Teh, W.-L., Hasegawa, H., Daughton, W., Hesse, M., Torbert, R. B., Burch, J. L., and Giles, B. L., "Measurement of the magnetic reconnection rate in the Earth's magnetotail," J. Geophys. Res.: Space Phys. **123**, 9150–9168, https://doi.org/10.1029/2018JA025713 (2018).

Parker, E. N., "The reconnection rate of magnetic fields," Astrophys. J. **180**, 247–252 (1973).

Shay, M. A., Drake, J. F., Rogers, B. N., and Denton, R. E., "The scaling of collisionless, magnetic reconnection for large systems," Geophys. Res. Lett. **26**, 2163–2166, https://doi.org/10.1029/1999GL900481 (1999).

Torbert, R. B., Burch, J. L., Giles, B. L., Gershman, D., Pollock, C. J., Dorelli, J., Avanov, L., Argall, M. R., Shuster, J., Strangeway, R. J., Russell, C. T., Ergun, R. E., Wilder, F. D., Goodrich, K., Faith, H. A., Farrugia, C. J., Lindqvist, P.-A., Phan, T., Khotyaintsev, Y., Moore, T. E., Marklund, G., Daughton, W., Magnes, W., Kletzing, C. A., and Bounds, S., "Estimates of terms in Ohm's law during an encounter with an electron diffusion region," Geophys. Res. Lett. **43**, 5918–5925, https://doi.org/10.1002/2016GL069553 (2016).

Torbert, R. B., Burch, J. L., Phan, T. D., Hesse, M., Argall, M. R., Shuster, J., Ergun, R. E., Alm, L., Nakamura, R., Genestreti, K. J., Gershman, D. J., Paterson, W. R., Turner, D. L., Cohen, I., Giles, B. L., Pollock, C. J., Wang, S., Chen, L.-J., Stawarz, J., Eastwood, J. P., Hwang, K.-J., Farrugia, C., Dors, I., Vaith, H., Mouikis, C., Ardakani, A., Mauk, B. H., Fuselier, S. A., Russell, C. T., Strangeway, R. J., Moore, T. E., Drake, J. F., Shay, M. A., Khotyaintsev, Y. V., Lindqvist, P.-A., Baumjohann, W., Wilder, F. D., Ahmadi, N., Dorelli, J. C., Avanov, L. A., Oka, M., Baker, D. N., Fennell, J. F., Blake, J. B., Jaynes, A. N., Le Contel, O., Petrinec, S. M., Lavraud, B., and Saito, Y., "Electron-scale dynamics of the diffusion region during symmetric magnetic reconnection in space," Science **362**, 1391–1395 (2018).

Torbert, R. B., Dors, I., Argall, M. R., Genestreti, K. J., Burch, J. L., Farrugia, C. J., Forbes, T. G., Giles, B. L., and Strangeway, R. J., "A new method of 3D magnetic field reconstruction," Geophys. Res. Lett. **47**, e2019GL085542, https://doi.org/10.1029/2019GL085542 (2020).

Tsiklauri, D., "A new fast reconnection model in a collisionless regime," Phys. Plasmas **15**(11), 112903 (2008).